

Thermoelectric Analysis of ZnSb Thin Films Prepared by ns-Pulsed Laser Deposition

A. Bellucci^{1,*}, M. Mastellone¹, A. Mezzi², S. Kaciulis², R. Polini^{1,3}, L. Medici⁴, and D. M. Trucchi¹

¹CNR-ISM, via Salaria km 29.3, 00015 Monterotondo Stazione, Rome, Italy

²CNR-ISMN, via Salaria km 29.3, 00015 Monterotondo Stazione, Rome, Italy

³Dipartimento di Scienze Tecnologie Chimiche, Università di Roma "Tor Vergata",
via della Ricerca Scientifica, 1, 00133 Rome, Italy

⁴CNR-IMAA, Contrada Santa Loja, 85050 Zona Industriale Tito Scalo, Potenza, Italy

Zinc antimonide (ZnSb) is a promising thermoelectric material for the temperature range 300–600 K. ZnSb thin films were prepared by nanosecond Pulsed Laser Deposition (PLD) to evaluate the performance of nanostructured films for thermoelectric conversion by the determination of the Power Factor. A study of the influence of structural, compositional and thermoelectric properties of thin films is reported as a function of different deposition parameters, such as repetition rate, pulse energy, and substrate temperature. The evaluation of a thin film ZnSb compound with excess Sb has been performed to verify the variation of the thermoelectric properties. The obtained results are reported and discussed in the 300–600 K temperature range.

Keywords: Thermoelectric Materials, ZnSb, Pulsed Laser Deposition, Nanostructuring.

1. INTRODUCTION

Among the renewable energy sources, thermoelectric devices are presently achieving a large interest, because, acting as solid-state heat engines, they can convert the waste heat available in many applications, such as industrial processes, micro-power sensors or concentrated solar power,¹ into electrical energy without the issues related to the use of thermodynamic heat engines. The lack of a wide diffusion of thermoelectric converters is the low efficiency of thermoelectric materials. Recent advances in the study of new thermoelectric materials envisaged the possibility to obtain high efficiency that could permit a large scale production of thermoelectric generators.^{2,3} A parameter that describes the ability of the material to efficiently perform energy conversion is its figure of merit ZT. Doping and nanostructuring represent the best routes to improve the properties of thermoelectric materials in order to tailor the electronic density of states and reduce the lattice thermal conductivity, respectively.⁴ The most intensively studied materials for thermoelectric applications are alloys based on bismuth and tellurium, that are toxic and expensive materials. Among the latest investigated compounds, ZnSb and Zn₄Sb₃ are promising low cost,

non-toxic thermoelectric materials, but large scale applications require development of fast and easy methods of material production.⁵ ZnSb should result more stable than Zn₄Sb₃ in the 300–600 K temperature range,^{6,7} for which only few efficient thermoelectric materials have been identified. Therefore, ZnSb can be considered as one of the best candidates in this temperature range, but it is mandatory to improve its thermoelectric properties to achieve suitable performances that are required for an industrial use. Low dimensional materials such as thin films are of great interest for construction of high performance thermoelectric devices.^{8,9} Thin films offer the prospects of significantly enhancing thermoelectric property of a material via quantum confinement effects, lattice mismatches, and/or thermionic emissions between layered multi-structures. For thin film semiconductors, the power factor $PF = S^2/\rho$, where S is the Seebeck coefficient and ρ the electrical resistivity, represents the “electronic” parameter describing the efficiency of thermoelectric power generation. This value depends on two competing material’s properties, Seebeck coefficient (S) and electrical resistivity (ρ) since S tends to drastically decrease, even if also ρ favorably decreases upon the increase of the carrier concentration. Pulsed Laser Deposition (PLD) can be considered a useful technique to produce thermoelectric films, as reported in

*Author to whom correspondence should be addressed.

some recent works.^{10–12} The ability to replicate the composition of the target material in the film is one of the benefits of PLD compared to other thin-film deposition techniques. In addition, PLD allows the production of native nanostructures with a high deposition-rate. This study aims at analyzing the influence of repetition rate, energy pulse, and deposition temperature on the compositional, morphological, and thermoelectric properties of ZnSb thin films. The addition of antimony (Sb) into the ZnSb matrix was performed by using a supplementary pure Sb target with the aim to evaluate the effect of a further metallic contribution into a multilayer structure on the thermoelectric PF.

2. EXPERIMENTAL DETAILS

The experimental setup of the PLD system consists of a nanosecond pulsed ArF excimer laser source (Lambda Physik COMPex 102, $\lambda = 193$ nm, pulse duration of 30 ns), focused at an angle of 45° on the target materials, and positioned in front of a stainless steel vacuum chamber evacuated by a turbo molecular pump (typical background pressure 1×10^{-6} mbar). Pulse repetition rate (RR) was varied between 10 and 18 Hz, the energy pulse (E_p) between 60 and 90 mJ, and the substrate temperature (T_{dep}) from RT to 300°C . ZnSb and Sb targets (commercial 1-inch diameter targets, 99.995% purity) were placed on a rotating holder during ablation to avoid cratering. Aluminum silicate, mirror polished, rod (1 mm diameter, 5 mm length) and flat plates ($10 \times 10 \times 1$ mm³), and silicon wafers (100) plates were used as deposition substrates. All the substrates were ultrasonically cleaned in *n*-hexane before mounting them in the vacuum chamber. They were positioned on a heated (from RT to 300°C) sample-holder at a distance of ~ 50 mm from the target. The overall deposition time was 90 min. After deposition, the specimens were processed to *in-situ* thermal annealing at 300°C for 2 h, with the aim to achieve film structural stability for the thermo-electronic characterizations.

The thickness of the thin films was measured by using an Alpha Step 500 profilometer (KLA Tenkor). The surface morphology was observed by field emission gun-scanning electron microscope (FEG-SEM, LEO Supra-35), equipped for energy dispersive X-ray spectroscopy (EDS, Oxford Instruments mod. INCA 300). The images were obtained under an acceleration voltage of 15 kV, with a magnification until 100 kX. X-ray Photoelectron Spectroscopy (XPS) analysis was carried out in an ESCALAB MkII spectrometer (VG Scientific, UK), equipped with Al K α excitation source and a 5-channeltron spectroscopic detection system. XPS measurements were carried out at 90° take-off angle and electrostatic lens mode resulting in 3 mm diameter of analysed sample area. For the depth profiling, an Ar⁺ beam of 2.0 keV energy and a sample current of 3×10^{-6} A were employed, which was rastered over a sample area of 3×3 mm².

X-ray micro-diffraction (micro-XRD) data, taken at grazing angle, have been acquired by a Rigaku D/MAX RAPID diffraction system equipped with a Cu K α source and operated at 40 kV and 30 mA. The data were collected in reflection mode using various grazing incidence “sample-to-beam” geometries and a beam collimator of $300 \mu\text{m}$.

The electrical resistivity was measured by the collinear four-probe technique, and the commercial MMR measurement system was used for measuring the Seebeck coefficient. The temperature-dependent electrical characterization was performed using the “four-contact-in-line-points probe” method, that allows the measurement of the film sheet resistance R_S . The film resistivity ρ was evaluated, once known the thickness t , by means of the formula: $\rho = \pi / \ln 2 \cdot R_S \cdot t$. Measurements have been performed by varying the temperature T under vacuum conditions to avoid film structural modifications and oxidation.

The temperature-dependent Seebeck coefficient measurements were performed in-plane using a commercial set-up, MMR technologies K-20 and SB-100 with a high-impedance amplifier (100 gain). Copper-constantan was used as a reference junction to monitor the temperature difference ΔT , that was fixed at 1.5 K by adjusting the heater power output. Initial delay was set to 3 min so that the temperature of the sample reaches equilibrium with the cooling stage, and the operation delay was adjusted to 30 s in order to achieve steady state conditions. Thermoelectric key properties were measured from room temperature (RT) up to 600 K in vacuum conditions ($< 5 \times 10^{-3}$ Torr) for all the samples.

This work aimed at finding the best experimental conditions for ns-PLD in terms of RR , E_p , and T_{dep} . The first set of samples was achieved by fixing $T_{\text{dep}} = 100^\circ\text{C}$ and $E_p = 80$ mJ and by varying RR to 10, 12, 14, 16, and 18 Hz. The second set was achieved by using the RR that allowed obtaining the higher PF (14 Hz), maintaining $T_{\text{dep}} = 100^\circ\text{C}$, and by varying E_p from 60 to 90 mJ. The third set was obtained in the best conditions for the increase of the PF (14 Hz and 80 mJ), and by varying T_{dep} to RT, 100, 200, and 300°C . Finally, a sample with a large enrichment of Sb was deposited at the best experimental conditions to evaluate the improvement of the thermoelectric properties. The study was carried out by evaluating morphological, compositional, and thermo-electronic properties of the different specimens.

3. RESULTS AND DISCUSSION

From the morphological point of view, the samples have similar properties that do not depend on the different experimental conditions. By analyzing Figure 1(a), the films grown by PLD have a low roughness (confirmed also by Atomic Force Microscopy, shown in Fig. 2), with the presence of several droplets of different size, ranging from tens of nanometers to few micrometers. Applying a

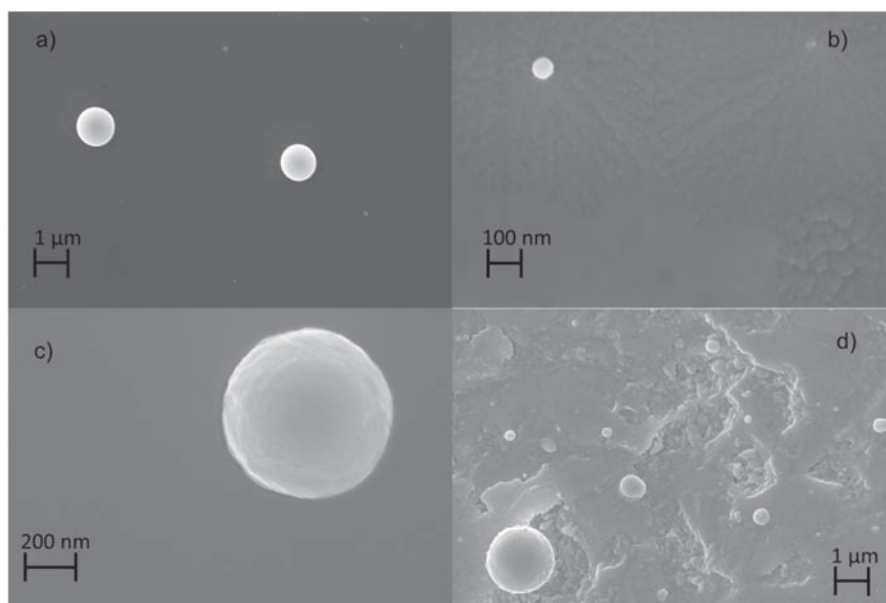


Figure 1. FEG-SEM images that show the surface morphology at increasing magnifications from (a–c). (d) Sample of the same batch that was mechanically scratched for investigation of the structure into the depth of the sample.

higher magnification (Fig. 1(b)) it is possible to observe the presence of wide areas characterized by grains of nanometric sizes. Fig. 1(c) reveals that also the droplets have a granular morphology. The presence of defects, such as nanocrystallite boundaries observed by SEM images (Fig. 1(d)), demonstrate nanostructuring, which should be beneficial to the reduction of the thermal conductivity. EDS spectra were obtained both on the flat film surface

and the micrometric-size droplets (Fig. 3). The differences on the spectra are only due to the predominant presence of the substrate (i.e., silicon) that is clearly more evident in the case of the flat film surface; in the case of the droplet, the size of these precipitates is in the order of some micrometers and is such that the silicon does not interfere in the analysis.

Compositional investigation by XPS did not indicate any important difference among the deposited samples of the three sets, with the identification of the Sb $3d_{5/2}$ peak positioned at a binding energy (BE) of (527.3 ± 0.1) eV and the Zn $2p_{3/2}$ peak positioned at BE = (1021.8 ± 0.1) eV.¹³ For clarification, an XPS depth profile is shown in Figure 4, where it is possible to observe a slight deviation from the stoichiometric ratio Zn:Sb = 1:1, with a composition Zn_xSb_y , where $x = 0.45$ and $y = 0.55$ for the different sets of samples. This deviation from the stoichiometry due to a Zn deficiency can be attributed to a larger Zn evaporation during target ablation process, caused by the higher volatility of Zn with respect to Sb.¹⁴ Anyway, this behavior was observed for all the deposited samples, independently of the different experimental conditions.

XRD spectra indicate the formation of very complex films, with the presence of different crystalline phases. In all the samples, both the ZnSb orthorhombic and hexagonal phase structures, and peaks related to the presence of Zn_4Sb_3 and Zn_3Sb_2 were identified. However, a significant trend was not identified as a function of the different experimental parameters. Figure 5 shows a typical spectrum obtained for the samples grown by PLD. Concerning

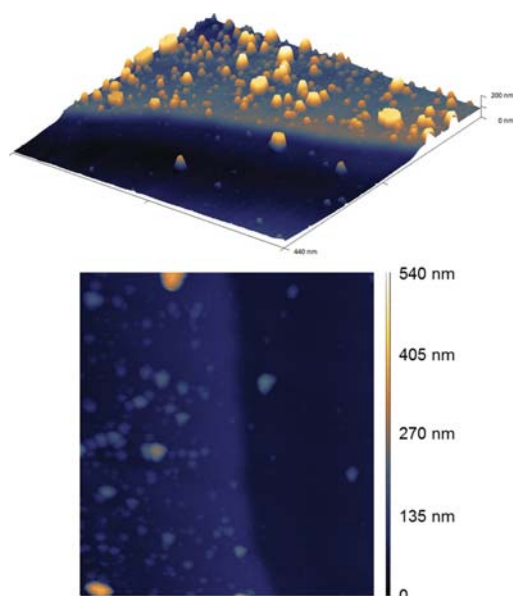


Figure 2. AFM images of film surface morphology.

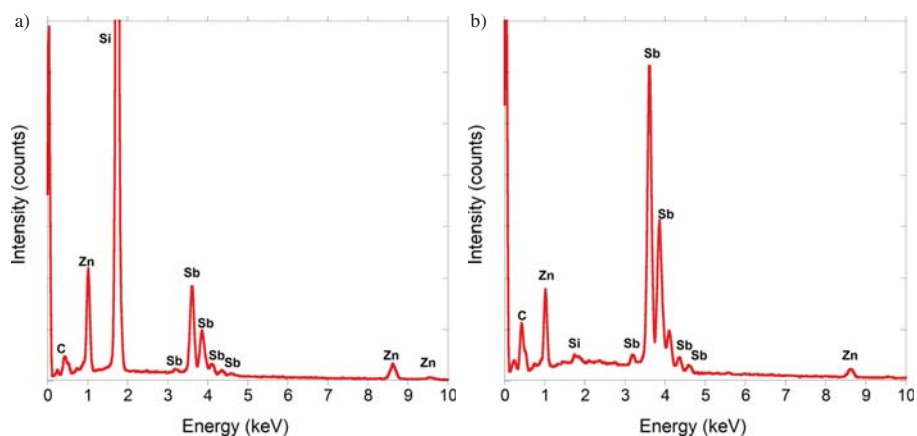


Figure 3. EDX spectra of one sample localized at: (a) the flat film surface (the peak related to silicon is predominant); (b) a single droplet (the peak related to silicon is negligible).

the size of the crystalline grains, obtained by the Scherrer's method¹⁵ analyzing the full width at half maximum (FWHM) of the more intense reflections of the different phases, values from 28 to 34 nm were found.

For the evaluation of the best experimental conditions, a thermo-electronic characterization was carried out. Figure 6 shows the temperature dependence of the PF on different repetition rate, energy pulse, and substrate temperature. According to Seebeck measurements, all the deposited samples show a *p*-type behavior, demonstrated by a positive Seebeck coefficient. This is in agreement with other works on both single-crystalline and polycrystalline ZnSb materials.^{16,17} For the sample reporting the highest PF, its electrical resistivity and Seebeck coefficient can be observed in Figure 7. The resistivity is typical of a semiconductor; the Arrhenius plot shows two temperature

dependent transport mechanisms, with different activation energies $E_{A,1} = 197 \pm 2$ meV and $E_{A,2} = 421 \pm 44$ meV for $T^{-1} < 0.002$ K⁻¹. We infer that the first activation energy can be ascribed to the filling of the Fermi level, localized above the maximum of the valence band (the samples have a *p*-type behavior). At higher temperatures, the involvement of a defect level contributes to the carrier transport and consequently causes an increase of conduction. The Seebeck coefficient increases up to 450 K, but the temperature increase leads to a reduction of *S* between 450 and 600 K. This is due to the increase of the electrical conductivity, whose relationship with the Seebeck coefficient is well-known for thermoelectric materials. In fact, the raise of temperature contributes to increase the electrically active carriers by promoting them in the valence

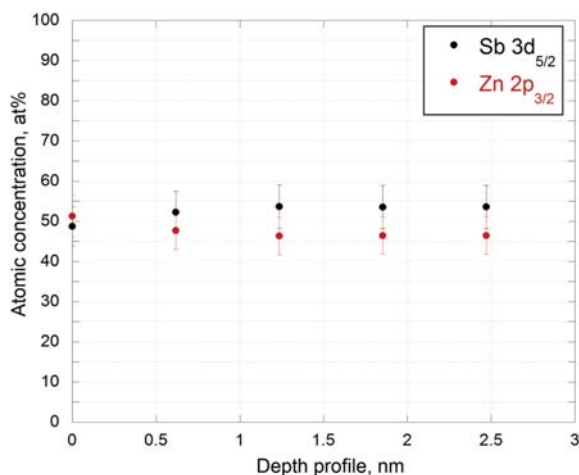


Figure 4. XPS depth profile of one sample at $RR = 14$ Hz, $E_p = 80$ mJ, $T_{dep} = 300$ °C. The etching time corresponds to a sputter depth of about 20 nm. All the deposited samples have the same compositional characteristic.

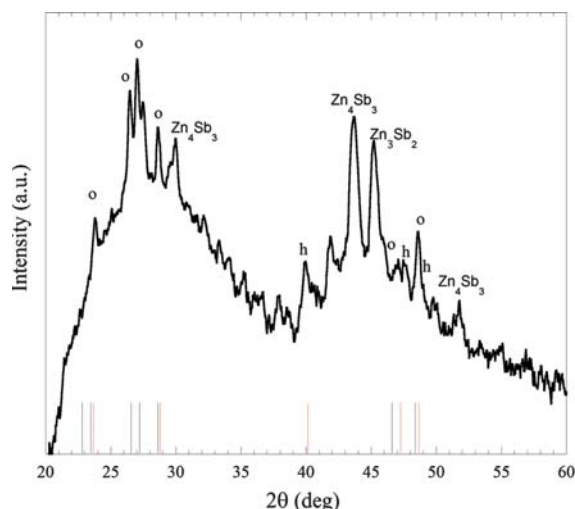


Figure 5. Typical XRD spectrum of ZnSb samples. The peaks were assigned by using the following JCPDS cards: o (orthorhombic ZnSb)-card 5-714; h (hexagonal ZnSb)-card 18-140; Zn₄Sb₃ (orthorhombic)-card 23-1017; Zn₃Sb₂ (orthorhombic)-card 23-1016.

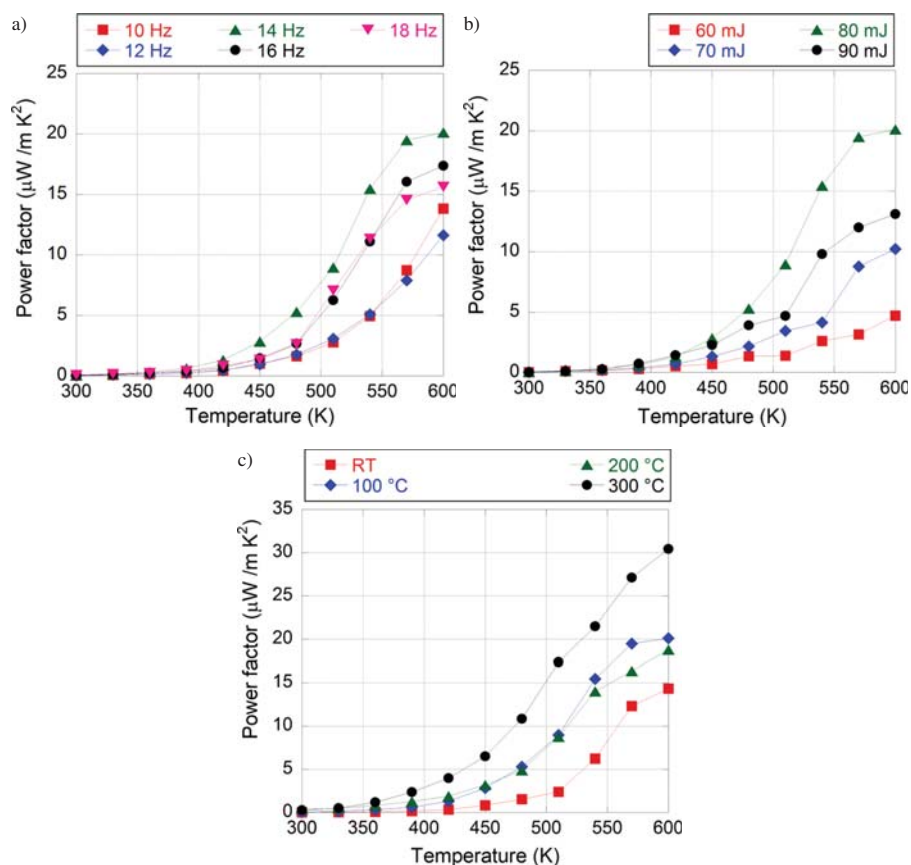


Figure 6. Power factor of the different sets of samples, as a function of temperature: (a) for different pulse RR ; (b) for different E_p ; (c) for different T_{dep} .

(or conduction) band, reducing the high-energy carriers able to be transported between hot and cold end of a material exposed to a temperature gradient. Anyway, the electrical conductivity results too low to make competitive these films.

Once the optimal set of pulse RR , E_p , and T_{dep} values was found, samples with a larger quantity of Sb, which was found to considerably decrease the electrical resistivity,¹⁸ were prepared in order to investigate the way of altering the electronic density of states in a multilayer

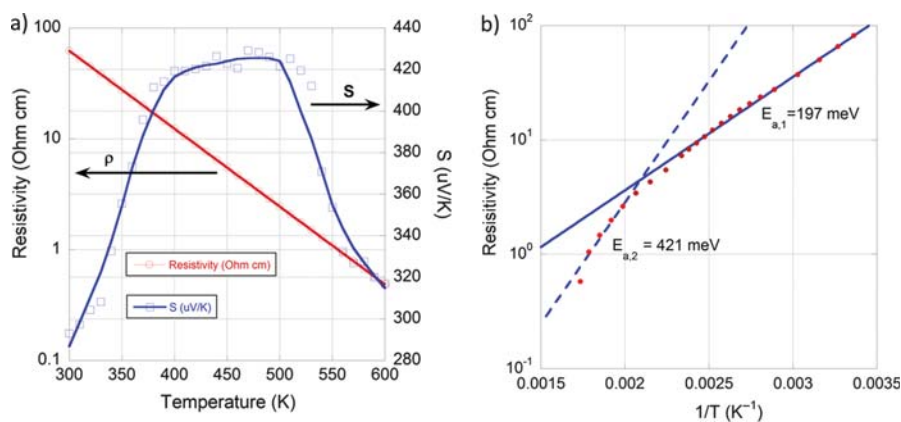


Figure 7. Specific data for the sample with the highest performance: (a) Seebeck coefficient and electrical resistivity as a function of temperature; (b) Arrhenius semi-logarithmic plot of the electrical resistivity for the calculation of the activation energy.

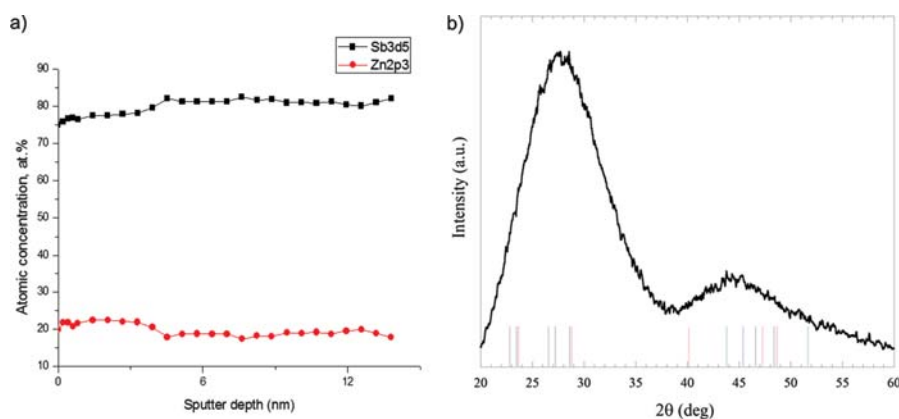


Figure 8. (a) XPS depth profile of one sample with Sb enrichment, that induces the formation of $\text{Zn}_{0.2}\text{Sb}_{0.8}$ compound. (b) XRD spectrum of amorphous $\text{Zn}_{0.2}\text{Sb}_{0.8}$ samples.

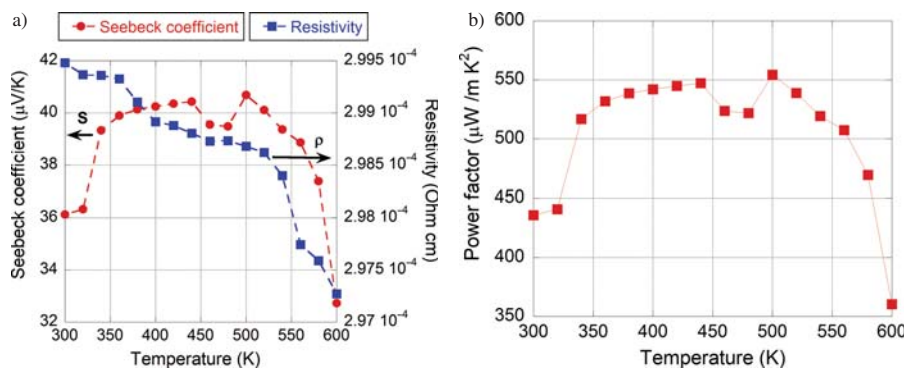


Figure 9. Thermoelectric properties of the sample $\text{Zn}_{0.2}\text{Sb}_{0.8}$. (a) Seebeck coefficient and electrical resistivity as a function of temperature; (b) PF as a function of temperature.

structure by PLD for ZnSb-based compounds. This enrichment led to a deviated stoichiometry such that the material assumes the unbalanced composition of $\text{Zn}_{0.2}\text{Sb}_{0.8}$ (as shown in Fig. 8(a)) and to an amorphous structure, revealed by XRD (Fig. 8(b)). Besides, the resistivity of the film was found to decrease from 6 down to 4 orders of magnitude than balanced ZnSb films in the same explored temperature range. From the thermoelectric point of view, this induces a significant improvement of the PF to values that are lower of a factor between 2 and 3 with respect to the best results reported in literature.^{13, 19} The resistivity trend is still of a semiconductor, but it is almost flat, denoting a behavior in proximity to a degenerate semiconductor or of a semimetal. It is known that deviations in stoichiometry can generate an appreciable amount of native defects or impurities, which can yield additional doping.²⁰ Anyway, the very low S , shown in Figure 9(a), due to a too high hole concentration, close to that of a degenerate semiconductor, represents a bottleneck to obtain a competitive PF. In the future, the introduction of possible dopants, such as Cu²¹ and Ag²², or a novel strategy based on deposition of the single targets of pure Zn and

Sb, will be investigated in order to obtain more complex structures and to enhance the thermoelectric properties of ZnSb-based thin films. In fact, the formation of multi-layer structure, together with the presence of nanocrystallites, can lead to a much higher Seebeck coefficient by means of carrier energy filtering²³ that represents the most proper way for decoupling the electrical conductivity from the Seebeck coefficient in order to effectively increase the material's thermoelectric power factor.

4. CONCLUSIONS

ZnSb thin films were prepared by PLD from ablation of bulk ZnSb target by varying different experimental parameters (pulse repetition rate, pulse energy, and substrate temperature). SEM analysis reveals a nanostructured aspect, and a low roughness. Compositional analysis demonstrates a good stoichiometry of Zn and Sb close to 1:1. The best conditions were found to be 14 Hz, 80 mJ, and 300 °C as RR , E_p , and T_{dep} , respectively. ZnSb-based thin films grown by PLD result promising for thermoelectric applications, as p -type materials. A Sb enrichment was tested to improve the thermoelectric performance of the films.

The sample resulted in a $\text{Zn}_{0.20}\text{Sb}_{0.80}$, but, despite the lack of a good stoichiometry that leads to a metallic-like behavior, its PF shows extremely higher values with respect to the pure ZnSb samples. Lowering the electrical resistivity induced a very large reduction of the Seebeck coefficient. In the future, a multilayer deposition starting from targets of Zn, Sb, and a third dopant element (Cr, Cu, or Ag) will be investigated.

References and Notes

1. A. Bellucci, P. Calvani, E. Cappelli, S. Orlando, D. Sciti, R. Yogev, A. Kribus, and D. M. Trucchi, *AIP Conf. Proc.* 1667, 02007 (2015).
2. G. J. Snyder and E. S. Toberer, *Nat. Mater.* 7, 105 (2008).
3. M. S. Dresselhaus, G. Chen, M. Y. Tang, R. Yang, H. Lee, D. Wang, Z. Ren, J.-P. Fleurial, and P. Gogna, *Adv. Mater.* 19, 1043 (2007).
4. J. R. Sootsman, D. Y. Chung, and M. G. Kanatzidis, *Angew. Chem. Int. Ed.* 48, 8616 (2009).
5. Y. Sun, M. Christensen, S. Johnsen, N. V. Nong, Y. Ma, M. Sillassen, E. Zhang, A. E. C. Palmqvist, J. Böttger, and B. B. Iversen, *Adv. Mater.* 24, 1693 (2012).
6. X. Song, P. H. M. Böttger, O. B. Karslen, T. G. Finstad, and J. Taftø, *Phys. Scr.* T148, 014001 (2012).
7. D. Eklöf, A. Fisher, Y. Wu, E.-W. Scheidt, W. Scherer, and U. Hausermann, *J. Mater. Chem. A* 1, 1407 (2013).
8. H. Bottner, G. Chen, and R. Venkatasubramanian, *MRS Bull.* 31, 211 (2006).
9. P. Fan, Z. Zheng, Z. Cai, T. Chen, P. Liu, X. Cai, D. Zhang, G. Liang, and J. Luo, *Appl. Phys. Lett.* 102, 033904 (2013).
10. A. Bellucci, E. Cappelli, S. Orlando, L. Medici, A. Mezzi, S. Kaciulis, R. Polini, and D. M. Trucchi, *Appl. Phys. A* 117, 401 (2014).
11. E. Cappelli, A. Bellucci, L. Medici, A. Mezzi, S. Kaciulis, F. Fumagalli, F. Di Fonzo, and D. M. Trucchi, *Appl. Surf. Sci.* 336, 283 (2015).
12. P. Mele, S. Saini, H. Honda, K. Matsumoto, K. Miyazaki, H. Hagino, and A. Ichinose, *Appl. Phys. Lett.* 102, 253903 (2013).
13. Z. Zheng, P. Fan, J. Luo, P. Liu, X. Cai, G. Liang, D. Zhang, and Y. Fan, *Intermetallics* 64, 18 (2015).
14. P. H. M. Böttger, K. Valsset, S. Deledda, and T. G. Finstad, *J. Electron. Mater.* 39, 1583 (2010).
15. H. P. Klug and L. E. Alexander, *X-ray Diffraction Procedures: For Polycrystalline and Amorphous Materials*, 2nd edn., Wiley-VCH, New York, United States of America (1974), pp. 424–434.
16. E. Justi, W. Rasch, and G. Schneider, *Adv. Energ. Conv.* 4, 27 (1964).
17. P. J. Shaver and J. Blair, *Phys. Rev.* 141, 649 (1966).
18. Y. Chen, G. Wang, X. Shen, T. Xu, R. P. Wang, L. Wu, Y. Lu, J. Li, S. Daia, and Q. Niea, *CrystEngComm* 16, 757 (2014).
19. K. Valsset, X. Song, and T. G. Finstad, *J. Appl. Phys.* 117, 045709 (2015).
20. P. H. M. Böttger, G. S. Pomrehn, G. J. Snyder, and T. G. Finstad, *Phys. Status Solidi A* 208, 2753 (2011).
21. Z. Zheng, P. Fan, J. Luo, G. Liang, P. Liu, and D. Zhang, *J. Alloy. Compd.* 668, 8 (2016).
22. D. Xiong, N. L. Okamoto, and H. Inui, *Scripta Mater.* 69, 397 (2013).
23. D. Narducci, E. Selezneva, G. Cerofolini, S. Frabboni, and G. Ottaviani, *J. Solid State Chem.* 193, 19 (2012).

Received: 22 March 2016. Accepted: 6 July 2016.